

# Formation time distribution of dark matter haloes: theories versus N-body simulations

W.P. Lin,<sup>12\*</sup> Y.P. Jing<sup>12</sup>, Lihwai Lin<sup>3</sup>

<sup>1</sup> *Shanghai Astronomical Observatory, the Partner Group of Max-Planck-Institute für Astrophysik, Nandan Road 80, Shanghai 200030, China*

<sup>2</sup> *Department of Astronomy & Beijing Astrophysics Center, Peking University, Beijing, 100871, China*

<sup>3</sup> *Department of Physics, National Taiwan University, Taipei*

## ABSTRACT

This paper uses numerical simulations to test the formation time distribution of dark matter haloes predicted by the analytic excursion set approaches. The formation time distribution is closely linked to the conditional mass function and this test is therefore an indirect probe of this distribution. The excursion set models tested are the extended Press-Schechter (EPS) model, the ellipsoidal collapse (EC) model, and the non-spherical collapse boundary (NCB) model. Three sets of simulations (6 realizations) have been used to investigate the halo formation time distribution for halo masses ranging from dwarf-galaxy like haloes ( $M = 10^{-3}M_*$ , where  $M_*$  is the characteristic non-linear mass scale) to massive haloes of  $M = 8.7M_*$ . None of the models can match the simulation results at both high and low redshift. In particular, dark matter haloes formed generally earlier in our simulations than predicted by the EPS model. This discrepancy might help explain why semi-analytic models of galaxy formation, based on EPS merger trees, under-predict the number of high redshift galaxies compared with recent observations.

**Key words:** methods: N-body simulations – cosmology:theory –dark matter – galaxies:haloes – galaxies: formation

## 1 INTRODUCTION

In the present preferred cosmological model, dark matter haloes form hierarchically through accretion and merging of smaller structures that grow from a Gaussian initial density field. This process is modeled by Press-Schechter theory (Press & Schechter 1974), which simply assumes a region with the mass over-density above a certain threshold will turn around and eventually collapse to form a bound object. Bond et al. (1991) developed an excursion set approach and used it to derive the number density of collapsed dark matter haloes more rigorously. Lacey & Cole (1993) used the excursion set theory to predict the merger rate at which small objects merge with each other to form larger objects, the conditional probability of its progenitor for a parent halo, as well as the survival probability of haloes. The predictions for the halo formation time distribution have been tested against N-body simulations [with  $128^3$  particles] (Lacey & Cole 1994). The conditional probability predicted by the excursion set theory (or EPS theory) has been widely used to plant merger trees (Kauffmann & White 1993;

Lacey & Cole 1994; Somerville & Kolatt 1999) so as to construct semi-analytical models of galaxy formation, and to study the clustering of dark matter halos (Mo & White 1996; Mo, Jing, & White 1997). However the EPS theory may fail to model the details of halo formation. For instance, the predicted mass function was not found to fit the simulation results very well (e.g. Lee & Shandarin 1998, Sheth & Tormen 1999). Tormen (1998) also reported that the excursion set predictions did not well fit the conditional mass function of sub-clumps in simulations. In addition, since the EPS theory failed to correctly describe the spatial distribution of small haloes in high resolution numerical simulations (Jing 1998, 1999; Lee & Shandarin 1999; Sheth & Tormen 1999), it may also fail to predict the halo formation time distribution. There are already some indications that the distribution of halo formation time in N-body simulations is not consistent with predictions (van den Bosch 2002a).

In fact, it is an approximation that the spherical collapse assumed in the EPS formalism. This process can be better modeled by a triaxial turn-around model (Bond & Myers 1996; Sheth, Mo & Tormen 2001; Sheth & Tormen 2002). One of such models is the so-called Ellipsoidal Collapse model or EC model. By taking the ellipsoidal collapse into account, Sheth, Mo and Tormen (2001)

\* *E-mail* address: linwp@center.shao.ac.cn, ypjing@center.shao.ac.cn, d90222005@ms90.ntu.edu.tw

found that the modified mass function can fit N-body simulations well. Sheth & Tormen (2002) pointed out that the conditional mass function was not universal since it was not consistent with their simulation results at every redshift. Another model is the Non-spherical Collapse Boundary model (or NCB model shortly) proposed by Chiueh & Lee (2001). It relates the halo formation to the collapse of the Zel'dovich pancakes. A recent version of the model was presented by Lin, Chiueh & Lee (2002). Both the EC and the NCB models were calibrated to fit the spatial two-point correlation function of halos (Jing 1998) and the mass function (Sheth & Tormen 1999) over a large range of halo mass.

This paper uses three sets of high resolution N-body simulations [with  $256^3$  or  $512^3$  particles] to study the distribution of halo formation redshift and make comparison with theory predictions. It is organized as follows. In section 2, we present the theory predictions by three analytical models. The simulations are described briefly in section 3 together with the method to find the halo formation redshift. There the simulation results are compared to the predictions. Main conclusions and discussion are given in section 4.

## 2 THE THEORETICAL PREDICTIONS FOR THE DISTRIBUTION OF HALO FORMATION REDSHIFT

The halo formation redshift is defined as the redshift at which its main progenitor has accumulated half of the halo mass. According to the EPS theory, the probability that a volume of mass  $M_1$ , which is within the region of mass  $M_2$  collapsed at redshift  $z_2$ , collapsed to form a progenitor at redshift  $z_1$  is given by the conditional probability function,

$$f_{S_1}(S_1, \delta_{c1}|S_2, \delta_{c2})dS_1 = \frac{(\delta_{c1} - \delta_{c2})}{\sqrt{2\pi}(S_1 - S_2)^{3/2}} \times \exp\left[-\frac{(\delta_{c1} - \delta_{c2})^2}{2(S_1 - S_2)}\right] dS_1 \quad (1)$$

$(S_1 > S_2, \delta_{c1} > \delta_{c2})$

where  $\delta_{c1} \equiv \delta_c(z_1)$  and  $\delta_{c2} \equiv \delta_c(z_2)$  (Lacey & Cole 1993). Here  $\delta_c(z)$  is the critical over-density required for the spherical collapse at redshift  $z$  (see eq.A6), and  $S_i \equiv \sigma^2(M_i)$  where  $\sigma(M_i)$  is the rms of the initial density fluctuation field smoothed on a scale which contains mass  $M_i$ , extrapolated using linear theory to the present time (see eq. A1).

Thus the conditional probability can be converted into the probability that a halo of mass  $M_2$  at redshift  $z_2$  has a progenitor in the mass range  $M_1$  to  $M_1 + dM_1$  at an earlier epoch  $z_1$  (i.e. the conditional mass function),

$$\frac{dp}{dM_1}(M_1, z_1|M_2, z_2)dM_1 = \left(\frac{M_2}{M_1}\right) f_{S_1}(S_1, \delta_{c1}|S_2, \delta_{c2})dS_1. \quad (2)$$

When using the excursion set model with ellipsoidal collapse (Sheth & Tormen 2002), the conditional probability should be replaced by following function,

$$f_{S_1}(S_1, z_1|S_2, z_2)dS_1 = \frac{|T(S_1, z_1|S_2, z_2)|}{\sqrt{2\pi}(S_1 - S_2)^{3/2}} \times \exp\left\{-\frac{[B(S_1, z_1) - B(S_2, z_2)]^2}{2(S_1 - S_2)}\right\} dS_1, \quad (3)$$

and

$$T(S_1, z_1|S_2, z_2) = \sum_{n=0}^5 \frac{(S_2 - S_1)^n}{n!} \frac{\partial^n [B(S_1, z_1) - B(S_2, z_2)]}{\partial S_1^n}$$

where the moving barrier  $B(S, z) = \sqrt{aS_*}[1 + \beta(S/aS_*)^\alpha]$  with  $S_* \equiv \delta_c^2(z)$ . The parameters are adopted from the best fitting of the mass function with N-body simulations,  $a = 0.707, \alpha = 0.485, \beta = 0.615$  (Sheth, Mo & Tormen 2001; Sheth & Tormen 2002).

While for the NCB model (Chiueh & Lee 2001), the conditional probability is a fitting formula (Lin et al. 2002) which reads as,

$$f_{S_1}(S_1, \delta_c(z_1)|S_2, \delta_c(z_2)) = f(\mu') \left| \frac{\partial \mu'}{\partial S_1} \right|. \quad (4)$$

Here

$$\mu' f(\mu') d\mu' = 2A(\kappa) \left(1 + \frac{1}{\mu'^{2q}}\right) \left(\frac{\mu'}{2\pi}\right)^{1/2} \exp\left(-\frac{\mu'}{2}\right) d\mu', \quad (5)$$

where

$$\mu' \equiv \frac{[\delta_c(z_1) - \delta_c(z_2)]\varepsilon(S_2, \kappa)}{(S_1 - S_2)^{1/2}}, \quad (6)$$

$$A = 0.322 + \frac{0.178}{\kappa}, \quad (7)$$

$$\varepsilon(S_2, \kappa) = \varepsilon(x) = 0.036x^4 - 0.309x^3 + 0.944x^2 - 1.060x + 1 \quad (8)$$

with  $x \equiv (\sqrt{S_2}/\delta_c(z_2) - 0.25)/\kappa$ , and  $q(\kappa)$  is required to satisfy the normalization condition

$$A = \sqrt{\frac{\pi}{2}} / \left( \sqrt{\frac{\pi}{2}} + \frac{\Gamma[-q + \frac{1}{2}]}{2 \times \frac{1}{2}(-q + \frac{1}{2})} \right). \quad (9)$$

Here  $\kappa$  is the separation of two boundaries, which is defined as  $\delta_c(z_1)/\delta_c(z_2)$ . Refer to the appendix of Lin et al. (2002) for further explanation of the fitting procedure for these parameters. Note that we use the uncorrected  $\mu'$  [eq.(29) of Lin et al.] rather than the corrected  $\mu'$  [eq.(33) of Lin et al.]. There are two reasons for this choice. First, the halo formation distribution is incorrectly normalized when using the corrected  $\mu'$ . Second, the correction for  $\mu'$  could be mass dependent.

Integrating equation (2) over the mass range  $M_2/2 < M_1 < M_2$  gives the probability  $P(< t_1)$  that its formation time is earlier than  $t_1$  or its formation redshift is larger than  $z_1$ . For a halo with mass  $M_0$  formed at the present, we set  $M_2 = M_0, t_2 = t_0, z_2 = z_0 = 0$ . Therefore the probability can be written as

$$P(< t_f) \equiv P(> z_f) = \int_{S_0}^{S_h} \frac{M_0}{M(S_1)} f_{S_1}(S_1|S_0) dS_1, \quad (10)$$

with  $S_h = S(M_0/2)$  (Lacey & Cole 1993). In this integration, the conditional probability functions (1), (4) and (5) are used for the EPS, EC and NCB models respectively. The accumulative probability  $P(> z_f)$  and thereby its redshift distribution  $\frac{dP}{dz_f}$ , can be calculated numerically.

The predictions of the halo formation redshift distribution for 3 typical masses are shown in Fig.1. Here we assume a LCDM cosmogony (with  $\sigma_8 = 0.9$ ) whose parameters will

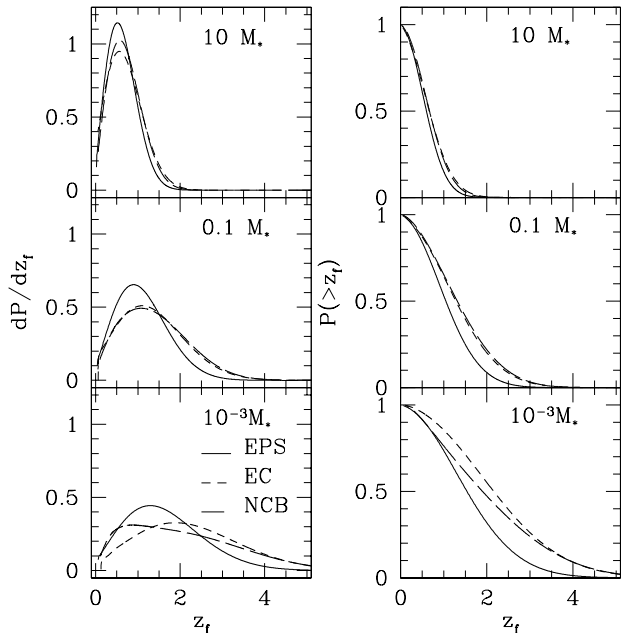


**Figure 1.** The model predictions of the formation redshift for haloes with mass of  $10^{-3}$ ,  $0.1$  and  $10M_*$ . The left panels give the differential probability distribution of the halo formation redshift, and the right panels give the accumulative probability of haloes formed at redshift higher than  $z_f$ .

be given in next section. The left and right panels show respectively the formation redshift distribution and the probability that a halo formed at redshift larger than  $z_f$ . The solid, dotted and dashed lines represent the EPS, EC and NCB predictions respectively. As can be seen, for haloes with a small mass of  $10^{-3}M_*$ , the predictions of the three models differ dramatically from each other. At low redshift the NCB prediction is close to the EPS one, however the predictions by the NCB and EC model are coincident at high redshift. For haloes with masses of  $0.1M_*$  and  $10M_*$ , the EC and NCB results only have a small difference. For the large mass, there is almost no big difference in the prediction among the three models. In general, the  $dP/dz_f$  profiles of the EC and NCB models are broader and have lower peaks than those of the EPS model. Compared to the EPS model, the EC or the NCB model predicts a larger fraction of haloes formed at high redshift and the EC model predicts a smaller fraction at low redshift.

### 3 SIMULATIONS

Three samples of N-body simulations are used to study the formation redshifts of dark haloes with mass ranging from  $10^{-3} M_*$  to  $8.7 M_*$ . Each simulation has at least 30 outputs, and can be used to trace the formation of a halo accurately. The cosmological model is the currently popular flat low-density model with the density parameter  $\Omega_0 = 0.3$  and the cosmological constant  $\Lambda_0 = 0.7$  (LCDM). The shape parameter of the linear density power spectrum is  $\Gamma \equiv \Omega_0 h = 0.2$ . The characteristic mass  $M_*$  is  $9.55 \times 10^{12} h^{-1} M_\odot$  for LCDMa, LCDMc simulations and  $1.66 \times 10^{13} h^{-1} M_\odot$  for

LCDMb simulations. Other parameters of the simulations are listed in Table 1, where  $\sigma_8$  is the amplitude of the power spectrum,  $N$  is the total number of particles in the simulation boxes,  $m_p$  is the mass of a particle and  $z_i$  is the initial redshift of the simulations.

The simulation data were generated on the VPP5000 Fujitsu supercomputer of the national Astronomical Observatory of Japan with a vectorized-parallel P<sup>3</sup>M code (Jing & Suto 1998, Jing & Suto 2002).

#### 3.1 The formation of small dark matter haloes

We use the LCDMa simulations to study the formation of small dark haloes. For each simulation, 56 out of the 169 outputs are used. Only those haloes with 100 particles or more at the present are included to assure a reliable identification of haloes (i.e., at the half-mass formation redshift, they have 50 particles at least). The haloes with more than 1200 particles will not be considered, since these haloes are not abundant enough to have a reliable determination of the distribution of the halo formation redshift. Thus the dark haloes we study here have a mass range between  $7.73 \times 10^9$  and  $9.28 \times 10^{10} h^{-1} M_\odot$  ( $\sim 10^{-3} - 10^{-2} M_*$ ). These haloes are “small” and represent the typical dark haloes of dwarf galaxies.

Dark matter haloes are identified with the spherical over-density method (Jing & Suto 2002). We adopt the following method to find the formation redshift of a halo. At the beginning we pick up a halo as a parent halo in the final output ( $z = 0$ ), and find out the particles within its virial radius. Then the member particles are traced in the outputs from high redshift to low redshift step by step. We calculate the fraction of the member particles in all progenitors, and select the progenitor with the maximum number of particles as the main progenitor. Generally, the members of the main progenitor will increase with time because of merging and accretion, although in a few circumstances its mass may decrease because of mass loss due to the tidal stripping by nearby haloes and/or unbound particles. When the main progenitor has reached at least half of the parent halo’s mass for the first time, we define the corresponding redshift as the formation redshift (half-mass formation redshift  $z_f$ ) of the selected parent. Alternatively, we can go along the merger tree from redshift 0 to high redshift, and we can define the formation redshift as the time when the mass of the main progenitor first drops below half of the parent halo’s mass. We find that these two definitions give almost an identical distribution of the halo formation time distribution<sup>1</sup>, as serious tidal stripping of the main progenitor happens only rarely. In the following, we will adopt the first definition and compare the simulations with the three analytical models.

The results are shown in Fig. 2(a)-(c). The solid points are the result measured from the simulations, and the vertical error bars present the  $1\sigma$  error of the mean value derived from the scatter between the realizations. The solid, short-dashed, and long-dashed lines are the predictions of the EPS, EC and NCB analytical models. For the model predictions, we plotted two lines for halo at the lower mass end (the

<sup>1</sup> There is only a slightly shift of the profile, but the conclusions change little.

**Table 1.** Model parameters for simulations

Model	$\sigma_8$	N	box-size $h^{-1}$ Mpc	$m_p$	time-steps $h^{-1} M_\odot$	$z_i$	outputs	realizations
LCDMa	0.9	$256^3$	25	$7.73 \times 10^7$	5000	72	169	2
LCDMb	1.0	$256^3$	100	$4.95 \times 10^9$	600	36	30	3
LCDMc	0.9	$512^3$	300	$1.67 \times 10^{10}$	1200	36	60	1

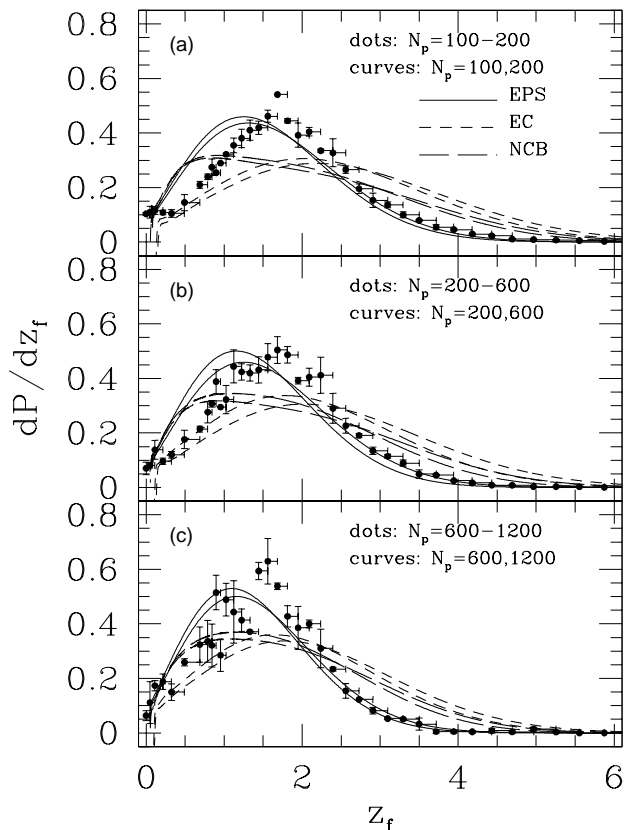


**Figure 2.** The distribution of the halo formation redshift for dwarf-galaxy like haloes. The points with error bars are the simulation results, and the lines are the predictions of the three analytical models. Different panels show the results for haloes of  $N_p$  particles. The total number of simulated haloes (2 realizations) used for the analysis are 2334/2295, 1747/1786, 505/456 for the results in panel (a)-(c) respectively.

curve with higher peak) and the higher mass end (the curve with lower peak) respectively. We plot both of them, because there may be a bias when using the prediction for the mean halo mass, as the formation probability is invariant in terms of  $\sigma(M)^2$  (rather than  $M$ ). For the narrow ranges of halo mass chosen in this study, this bias is sufficiently small as the predictions at the upper and lower mass limits are very close. To elucidate another possible bias caused by the limited output resolution, we also add a right-hand “error” bar for the simulation results. This bias is introduced by the fact the halo formation time in simulation is measured to be the redshift at which the fraction of the member particles is larger than 0.5 for the first time, however the real formation

redshift should fall between this output and the earlier one. This uncertainty is shown by the right-hand “error” bars.

As the figure shows, at low redshift ( $\leq 1$ ) the EPS and NCB models predict more haloes than the simulations, while the EC predictions are consistent with the simulation results. However at high redshift, the EPS model fits the simulation results better than the EC and NCB models. In every panel, the formation redshift distribution of the simulations peaks at a higher redshift than the EPS prediction<sup>2</sup> and has a narrower profile (but with a higher peak) than the EC and NCB predictions.

### 3.2 The formation of sub- $M_*$ dark matter haloes

The LCDMb simulations are used to study the formation of sub- $M_*$  dark haloes. Again the number of particles in a halo spans from 100 to 1200, or the corresponding halo mass ranges from  $4.95 \times 10^{11} h^{-1} M_\odot$  to  $5.94 \times 10^{12} h^{-1} M_\odot$  (i.e.  $\sim 0.03-0.36 M_*$ ). The definition of haloes is slightly different from that used in the last subsection. Here distinct haloes were found using the FOF method with a bonding length 0.2 times of the mean particle separation. We have tested the results for one realization against the two halo identification algorithms, and found that the two identifications give nearly identical results. We calculate the halo formation redshift as in the last subsection for the 30 outputs, and plot the results in Fig.3.

The results found for the sub- $M_*$  haloes are quite similar to those for smaller haloes, but we can see continuous changes with halo mass of the model predictions relative to the simulation results. The EPS model predicts too many haloes of low formation redshifts again, while the EC and NCB models predict relatively well the fraction of these haloes. On the other hand, the EC and NCB models predict too many haloes of high formation redshift. Note that for the mass range chosen here the EC and NCB predictions are close to each other (cf. Fig.1).

### 3.3 The formation of large dark matter haloes

We use a simulation (LCDMc) with  $512^3$  particles (Jing 2002) to study the formation of large dark haloes. The corresponding halo mass ranges from  $1.67 \times 10^{12} h^{-1} M_\odot$  to  $8.35 \times 10^{13} h^{-1} M_\odot$  ( $\sim 0.17-8.74 M_*$ ). We did the same

<sup>2</sup> For the theoretical predictions of the halo formation redshift, a test on the infrared cut-off of wavenumber  $k$  due to a finite simulation box has been done. The cut-off can modify the  $M-\sigma^2(M)$  relation so that it can change the distribution of the halo formation redshift. However, for the small haloes considered here, the wavenumber cutoff has negligible effect on their formation redshift.

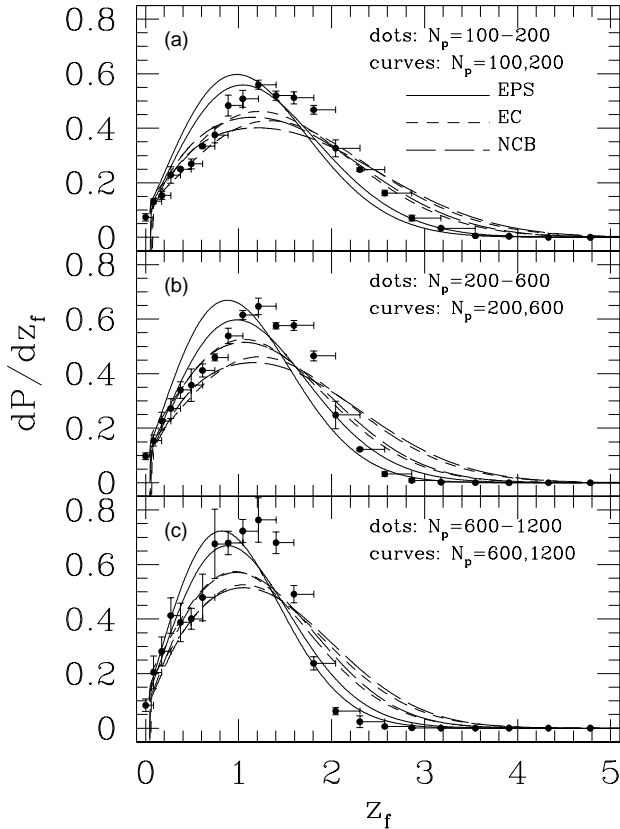


**Figure 3.** The same as Fig.2, but for sub- $M_*$  haloes. The total number of simulated haloes (3 realizations) used for the analysis are 3577/3487/3607, 2698/2549/2619, 758/773/724 for the results in panel (a)-(c) respectively.

analysis as the last subsection, and plot the results in Fig.4. Since the LCDM simulation has only one realization, no error bars are plotted for  $dP/dz_f$ . However, because of the high mass resolution, the population of haloes within each mass range is so large that the random fluctuation among the bins is small. This also makes us be able to extend the analysis to massive haloes with up to 5000 member particles.

Figure 4 continuously shows the change of the formation redshift distribution with the halo mass. The pattern of the differences between simulation results and predictions is similar to that of small dark haloes. For the very massive haloes [Fig.4(e)], the differences among the three models are small, and they agree with the simulation results reasonably well. The results shown in Fig. 3(c) has mass range of  $0.18 - 0.36M_*$  which is almost the same as that of Fig. 4(a) (whose mass range is  $0.17 - 0.35M_*$ ), even though  $\sigma_8$  used in these simulations are slightly different. Therefore, these two results can be compared for the same population of haloes with different mass resolutions. As can be seen, the results are consistent within the errorbars, though the population in the LCDM simulation appears to form slightly later than that in the LCDM.

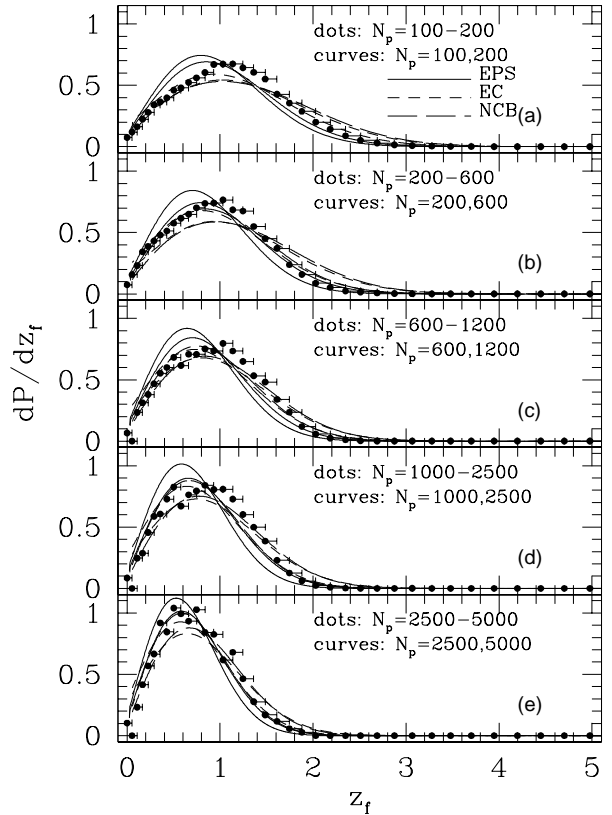


**Figure 4.** The same as Fig.2, but with  $512^3$  particles in the simulation box and for haloes with mass  $\geq 0.17M_*$ . The total number of simulated haloes used for the analysis are 35381, 25418, 7060, 5334, and 1840 in panels (a)-(e) respectively.

### 3.4 Resolution tests

We consider haloes with at least 100 particles, so the identification of the haloes is generally secure. There are still a couple of issues one should consider about the simulation resolutions. If the simulations are not started sufficiently early, some non-linear collapse could be missed or delayed, and the initial distribution of particles might still have an appreciable effect at the high redshift. Another worry is that some low mass haloes may be missed because of the force softening adopted in the simulations. To check these issues, we performed another two simulations that were run until  $z \simeq 3.18$ . These two simulations have the same model parameters and the same initial fluctuations (including the phase) as the first realization of the LCDM simulations, but one simulation was started at an earlier epoch  $z_i = 72$  and the other adopts force softening  $\eta = 78$  kpc that is twice large of the value used in the LCDM simulation (39 kpc). The two simulations have also the data output at  $z \simeq 4.78$ . In Figure 5, we plot the mass functions  $\nu f(\nu)$  of haloes at both redshifts for these two simulations, and compared them with that of the corresponding LCDM realization, where  $\nu \equiv [\delta_c(z)/\sigma(m)]^2$ . Except for very massive haloes that are rare objects (so their mass functions have large statistical fluctuations), the agreement of the mass functions among the three simulations is nearly perfect, especially for the mass range of 50 to 600 member particles that we are inter-

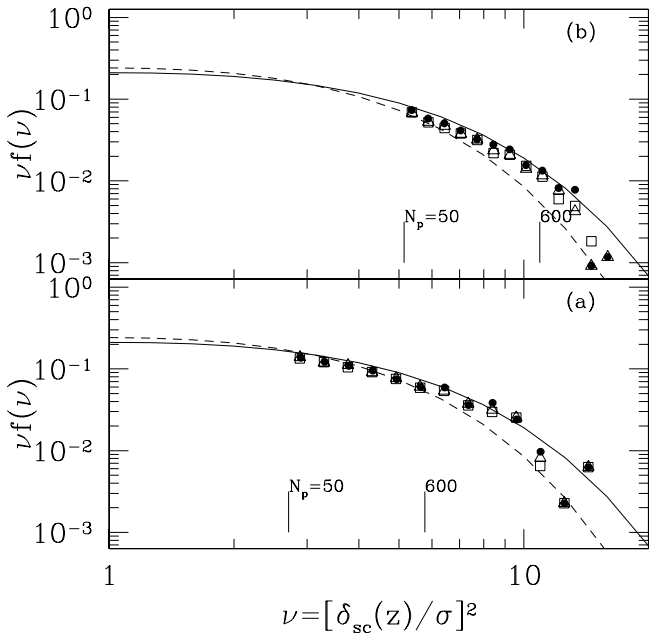


**Figure 5.** (a) The mass function of haloes at  $z \sim 3.18$  in the three simulations: the dots for the simulation with  $z_i = 72$ , the triangles for the simulation with the force softening 78 kpc, and the open squares for the first LCDMB realization. The lines labeled with  $N_p$  indicate the  $\nu$  values corresponding to 50 and 600 member particles respectively. The dashed line and solid line represent the predictions by the EPS model and the EC model. (b) The same as (a), but at  $z \sim 4.78$ .

ested in this paper. Therefore we conclude that our results here are robust to the starting redshifts and to the force softening of the simulations.

#### 4 DISCUSSION AND SUMMARY

This work was initially motivated by the fact that the semi-analytical models of galaxy formation which were constructed based on the EPS theory for the merger tree predict systematically redder colours for dwarf galaxies than the observations of faint blue galaxies (van den Bosch 2002b). It is known that the EPS theory fails accurately describing the mass function and the spatial correlation of small haloes ( $M \ll M_*$ , Jing 1998, Lee & Shandarin 1998, Sheth & Tormen 1999). This difficulty motivated many theorists to reformulate the formation of haloes, and reproduce the mass function as well as the spatial two-point correlation function of haloes in numerical simulations (Sheth et al. 2001; Chiueh & Lee 2001, Lin et al. 2002). It is therefore interesting to test if the EPS theory, or the alternative models can correctly predict the distribution of the halo formation time (which is more closely related to the problem of faint blue galaxies).

With the help of a large set of high-resolution N-body simulations, we have found various degrees of success and failure for the analytical models at different halo mass. This is not unexpected since the excursion set approaches roughly model the growth of haloes but overlook some factors which

could be important. For example, the models overlook the correlation between the fluctuations on different scales, do not include tidal striping, etc. If the conditional mass function has problems, the merger trees constructed upon it may not correctly describe the growth of haloes (especially for small haloes) and therefore should be used with caution in galaxy formation models. We suggest that future studies of the conditional mass function should be pushed toward lower mass end using simulations with high mass resolution (like those used here).

The implications of our results for the problem of the faint blue galaxies are quite clear. If the merger trees used by the semi-analytical models are replaced by the merger trees from the simulations, one would expect that the dwarf galaxies will become generally redder, which contradicts with the observations more seriously. There are several ways to solve this discrepancy. First, the observed faint blue galaxies may not constitute a representative sample of small haloes. This could happen if many of red dwarf galaxies, because of their low star formation rate, have escaped from being detected. Second, star formation within small haloes is significantly delayed due to heating or re-ionization (see Mo & Mao 2002, and reference therein). Third, faint blue galaxies may experience a recent interaction with nearby galaxies, which will trigger star formation. We have traced the trajectories of small haloes, and found that about 10% ~ 15% of the small haloes once pass the central part (with distance less than half of a virial radius) of a bigger halo which is at least 3 times more massive than the small one. These haloes should have experienced a strong interaction. If gas in the small halo would not be stripped off, these strong interactions could trigger star formation and change the colour of the dwarf galaxies to blue. However these processes are so complex that more efforts are needed to work out the problem of dwarf galaxies.

From the results of the LCDMB simulations, we found an earlier formation time for sub- $M_*$  haloes (about  $10^{12}$  solar mass) than the EPS prediction. This may indicate that galaxies are formed slightly earlier in the numerical simulations than in the EPS model. This result can explain a recent finding of Cimatti et al. (2002). Cimatti et al. measured the redshift distribution of galaxies with  $K < 20$ , and compared it with the predictions of semi-analytical models of galaxy formation based on the EPS merger trees. They found that the galaxies in the observation formed earlier than in the galaxy formation models of about 0.3 in redshift. Qualitatively this can be seen in our Figure 3. Of course, the formation times of haloes and galaxies are not the same thing, but they should have a similar trend.

There seems to be discrepancy between our results and those of van den Bosch (2002a) who found that the formation time distribution of the haloes in the GIF simulation deviates from the EPS prediction more severely at a larger mass. In fact, he checked for the haloes in two mass ranges:  $5.6 \times 10^{11} \leq M \leq 1.1 \times 10^{12} h^{-1} M_\odot$  and  $2.0 \times 10^{12} \leq M \leq 2.0 \times 10^{14} h^{-1} M_\odot$  (his Figure 4), corresponding to the number of particles  $40 \leq N_p \leq 80$  and  $140 \leq N_p \leq 14000$  respectively. The number of haloes in each mass bin is dominated by the lower mass end, especially in the larger mass bin. For the small haloes of  $M \leq 1.1 \times 10^{12} h^{-1} M_\odot$ , it is likely that his formation time is underestimated (i.e. formation delayed) because of the lim-

ited resolution, and so his agreement with the EPS theory becomes better. His result for large haloes should be compared with the middle panel of our Figure 3 (according to the effective mass). This comparison clearly shows that his results agree well with ours.

In summary, none of the predictions by the EPS, EC and NCB model can match the simulation results at both low and high redshift. This discrepancy implies that the theoretical mass conditional function needs further improvement. Our results may have an important impact on the models of galaxy formation. The “blue-color” problem of dwarf galaxies can hardly be solved solely by the gravitational interaction between dark matter. For sub- $M_*$  haloes, an increase of formation redshift by  $\sim 0.3$  relative to the EPS model may relieve the difficulty of the semi-analytical models to explain the recent observation of K20 galaxies (Cimatti et al. 2002) at high redshift.

## ACKNOWLEDGMENTS

The authors would like to thank Gerhard Börner, Houjun Mo, Tzihong Chiueh and Joungun Lee for useful discussions, and the anonymous referee for helpful comments and suggestions. YPJ is supported by NSFC No.10125314 and NKBRFSF G19990754. WPL acknowledges the grants provided by NKBRFSF G1999075402, NFSC No.10203004 and Shanghai NFS No. 02ZA14093.

## APPENDIX A: THE LINEAR GROWTH OF THE DENSITY PERTURBATION

We assume that the universe is dominated by cold dark matter. The mass  $M$  of a halo is related with the co-moving length scale  $r_0$  using a top-hat filter in real space  $M = (4\pi/3)\pi r_0^3 \rho_0$ , where  $\rho_0$  is the co-moving mean mass density of the Universe. The variance of the density fluctuations, smoothed over a region of mass  $M$ , is given by

$$\sigma^2(r_0) = \int_0^\infty \frac{dk}{k} k^3 P(k) W^2(kr_0) \quad (\text{A1})$$

where  $W(kr_0)$  is the window function for top-hat filtering

$$W(kr_0) = 3 \left[ \frac{\sin(kr_0)}{(kr_0)^3} - \frac{\cos(kr_0)}{(kr_0)^2} \right]. \quad (\text{A2})$$

The power spectrum at present is given by

$$P(k) \propto k T^2(k) \quad (\text{A3})$$

which uses the self-similar primordial density spectrum with index  $n = 1$ . For the transfer function, we have used

$$T(k) = \frac{\ln(1 + 2.34q)}{2.34q} \times \left[ 1 + 3.89q + (16.1q)^2 + (5.46q)^3 + (6.71q)^4 \right]^{-1/4} \quad (\text{A4})$$

and

$$q \equiv \frac{k}{\Gamma h^{-1} \text{Mpc}} \quad (\text{A5})$$

(Bardeen et al. 1986). In practice  $\sigma^2(r_0)$  was calculated up to an overall constant which is fixed by the choice of  $\sigma_8 \equiv \sigma(8h^{-1} \text{Mpc})$ .

Collapsed halos are taken to be regions in the linear density field with the density contrast greater than some critical density contrast,  $\delta_c$ . In practice we take into account of the linear growth by holding the variance  $\sigma$  fixed and increasing the density thresholds at high redshift,

$$\delta_c(t(z)) = (1+z) \frac{g(\Omega_0)}{g(\Omega(z))} \delta_c. \quad (\text{A6})$$

The growth rate can be approximated as

$$g(\Omega(z)) = \frac{5}{2} \Omega \left[ \frac{1}{70} + \frac{209}{140} \Omega - \frac{\Omega^2}{140} + \Omega^{4/7} \right]^{-1} \quad (\text{A7})$$

and

$$\Omega(z) = \Omega_m \frac{(1+z)^3}{1 - \Omega_m + (1+z)^3 \Omega_m} \quad (\text{A8})$$

for a flat  $\Lambda$  universe (Carroll, Press & Turner 1992).

## REFERENCES

- Bardeen J., Bond J.R., Kaiser N., Szalay A.S., 1986, ApJ, 304, 15  
 Bond J.R., & Myers S., 1996, ApJS, 103, 1  
 Bond J.R., Cole S., Efstathiou G., Kaiser N., 1991, ApJ, 379, 440  
 Carroll S.M., Press W.H., & Turner E.L., 1992, ARA&A, 30, 499  
 Chiueh T., & Lee J., 2001, ApJ, 555, 83  
 Cimatti A., et al., 2002, A&A Letter, 391, L1  
 Jing Y.P., 1998, ApJ, 503, L9  
 Jing Y.P., 1999, ApJ, 515, L45  
 Jing, Y. P. 2002, MNRAS, 335, L89  
 Jing Y.P., & Suto Y., 1998, ApJ, 494, L5  
 Jing Y.P., & Suto Y., 2002, ApJ, 574, 538  
 Kauffmann G., & White S.D.M., 1993, MNRAS, 261, 921  
 Lacey C., & Cole S., 1993, MNRAS, 262, 627  
 Lacey C., & Cole S., 1994, MNRAS, 271, 676  
 Lee J., & Shandarin S.F., 1998, ApJ, 500, 14  
 Lee J., & Shandarin S.F., 1999, ApJ, 517, 5L  
 Lin L., Chiueh T., & Lee J., 2002, ApJ, 574, 527  
 Mo H.J., & Mao S., 2002, MNRAS, 333, 768  
 Mo, H. J. & White, S. D. M. 1996, MNRAS, 282, 347  
 Mo, H. J., Jing, Y. P., & White, S. D. M. 1997, MNRAS, 284, 189  
 Press W., & Schechter P., 1974, ApJ, 187, 425  
 Sheth R.K., Mo H.J., & Tormen G., 2001, MNRAS, 323, 1  
 Sheth R.K., & Tormen G., 1999, MNRAS, 308, 119  
 Sheth R.K., & Tormen G., 2002, MNRAS, 329, 64  
 Somerville R.S., & Kolatt T.S., 1999, MNRAS, 305, 1  
 Tormen G., 1998, MNRAS, 297, 648  
 van den Bosch F.C., 2002a, MNRAS, 331, 98  
 van den Bosch F.C., 2002b, MNRAS, 332, 456